Imaging at the Nano-scale: State of the Art and Advanced Techniques

Bernardo D. Aumond[1], Osamah M. El Rifai[2], and Kamal Youcef-Toumi[3]
[1]Mechanical Engineer, Surface Logix, Massachusetts
[2]Research Scientist, Department of Mechanical Engineering, MIT
[3]Professor, Department of Mechanical Engineering, MIT, SMA Fellow
email:BAumond@surfacelogix.com, osamah@mit.edu, youcef@mit.edu

Abstract— Surface characteristics such as topography and critical dimensions serve as important indicators of product quality and manufacturing process performance especially at the micrometer and the nanometer scales. This paper first reviews different technologies used for obtaining high precision 3-D images of surfaces, along with some selected applications. Atomic force microscopy (AFM) is one of such methods. These images are commonly distorted by convolution effects, which become more prominent when the sample surface contains high aspect ratio features. In addition, data artifacts can result from poor dynamic response of the instrument used. In order to achieve reliable data at high throughput, dynamic interactions between the instrument's components need to be well understood and controlled, and novel image deconvolution schemes need to be developed. Our work aims at mitigating these distortions and achieving reliable data to recover metrology soundness. A summary of our findings will be presented.

Index Terms— Imaging, Atomic Force Microscope, Deconvolution, Stereo Imaging, Piezoelectric, Model, Performance Limitations, Scan Parameters, Creep, Hysteresis, Calibration

I. INTRODUCTION

Surface characteristics such as topography and critical dimensions, roughness and areal density, shape and location of defects often serve as important indicators of product quality and manufacturing process performance. For such reasons, surface characterization procedures are of primary importance in a wide range of technological fields and across industries. In addition, high precision characterization has played an increasingly important role as the required dimensions of semiconductor and other micro-fabricated devices continue to shrink into the micrometer and nanometer domains [1]. Several tools are now available for this task. Each of these tools has its strengths and weaknesses. In this paper, a review of the main imaging tools will be presented. The paper will focus on using AFM in nano-scale imaging and will address technological challenges encountered. A summary of our research on mitigating these challenges will be presented.

The paper is organized as follows. In Section II, a review of the main imaging tools is presented. Technical challenges encountered with AFM imaging due to AFM dynamics and convolution are discussed in Section III. A summary of our work on addressing challenges related to AFM dynamics are given in Section IV. Section V presents a new image deconvolution scheme. Finally, conclusions are given in Section VI.

II. IMAGING AT THE NANO-SCALE

There exist several imaging techniques that allow for the extraction of metrology data from a surface. These methods may differ in 1) their destructive or non-destructive nature, 2) the achievable lateral resolutions, 3) the achievable vertical resolution, 4) the vertical and lateral ranges 5) and the types of surfaces that can be probed with respect to their conductivity, reflectivity and magnetic natures.

One common low resolution imaging technique is the conventional stylus. It consists of a stylus with a sharp tip that is mechanically dragged along the surface. The deflection of the hinged stylus arm is measured and recorded as the surface profile. The use of a hinged stylus arm allows measurement of very rough surfaces (peak-to-peak heights greater than $1\,mm$ [2]). On the other hand, since the hinged stylus arm is partially supported by the stylus itself, physical rigidity limits the minimum stylus tip radius and hence the lateral resolution to about $0.1\,mm$. Probe-to-surface contact forces range from $10^{-3}\,N$ to $10^{-6}\,N$ and vertical resolution is in the order of 1 to $5\,nm$ in certain cases in "quiet" setups.

In optical profilometry, many different optical phenomena such as interference and internal reflection can be utilized. The most popular technique is based on phase-measuring interferometry, in which a light beam reflecting off the sample surface is interfered with a phase-varied reference beam. The surface profile is deduced from the fringe patterns produced. With a collimated light beam (i.e. the light is made to travel in parallel lines) and a large photodetector array, the entire surface can be profiled simultaneously. This and other conventional optical methods are limited in lateral resolution by the minimum focusing spot size of about $0.5\,\mu m$ (for visible light). In addition, measurement values are dependent on the surface reflectivity of the material being profiled. Vertical resolution is in the $1\,nm$ range.

One of the most popular imaging technologies for critical dimension assessment in the nano regime is scanning electron microscopy (SEM). This methodology relies on the phenomenon of electron back scattering off a surface. The resolution of SEM is dictated by the minimum focusing spot of the electron beam and the volume of interaction since the detected electrons emerge not from the free surface but from shallow penetration depths. Therefore, thin and sharp samples are difficult to image with SEM because the penetration depth may exceed the dimensions of the sample. In addition, SEM is only applicable to conductive samples. Therefore non conductive specimens must be pre coated with a metal film, which may change the sample dimensions. Lateral resolutions can reach $1\,nm$.

Another class of imaging devices known as scanning probe microscopes (SPM) can meet sub-nanometer lateral and vertical resolution requirements. In these microscopes, a very sharp tip at a very close spacing to the surface is moved over the surface using a piezoelectric actuator. The types of SPM currently available include atomic force microscope (AFM), scanning tunneling microscope (STM), scanning near-field optical microscope (SNOM), scanning capacitance microscope, scanning thermal microscope and magnetic force microscope. These variants of the same technology differ from each other by the physical variable that is used to assess the topographic features of the sample.

In contact mode AFM, a cantilever beam mounted microstylus is moved relative to the sample surface while in contact with the sample. The displacement of the piezoelectric actuator is taken to be a measure of the surface topography. Atomic force microscopy offers ultra-high lateral and vertical resolutions (less than $1\,nm$ is possible), however, the maximum surface roughness that can be profiled is much less than that of the conventional stylus due to the limited actuator range. Probe-to-surface contact forces range from $10^{-8}\,N$ to $10^{-11}\,N$.

In the non-contact AFM, long range van der Waals forces are measured by vibrating the cantilever (on which the probe tip is mounted) near its resonance frequency and detecting the change in the vibrational amplitude of the beam due to a change in the force gradient (i.e. because of changes in the surface profile). The non-contact atomic force microscope offers non-invasive profiling, however, the technique has some disadvantages when compared to contact mode AFM. First, van der Waals forces are hard-to-measure weak forces, hence the microscope is more susceptible to noise. Secondly, the probe tip must be servoed to a fixed height above the sample (typically a few nanometers) - this must be done slowly to avoid crashing the tip. Thirdly, since the tip is always floating above the surface, the effective tip radius is increased and hence the achievable lateral resolution is decreased. A variant of this technique is the intermittent contact mode AFM where the tip is vibrated and lightly taps the surface, close to the resonant frequency of the cantilever. Such an approach is applied to soft and biological samples that could be damaged by the contacting probe.

For STM, quantum tunneling current between the probe tip and sample is measured. The STM is attractive because it is a non-contact device (i.e. no surface damage, potential for high speed profiling) with the highest resolution of all the scanning probe microscopes, however, it can only be used on electrically conducting surfaces.

In SNOM, the focusing limit of conventional far-field optics is bypassed by bringing a $20\,nm$ diameter light aperture approximately $5\,nm$ from the surface; the resulting transmitted or reflected light is collected to form an image. SNOM technology is still very much in the research stage - the minimum achievable lateral resolution so far ($12\,nm$) has been limited by the ability to form the light aperture reproducibly [3].

With the scanning thermal microscope, the measured temperature of an AC current heated tip is a function of gap spacing [3]. The magnetic and electrostatic force microscopes measure the force due to a magnetic and electrostatic potential field, respectively [3]. The electrostatic force microscope is different from the scanning capacitance microscope [3], which measures the capacitance between the probe tip and the sample. These methods do not measure topography directly - the sensed quantity is actually a function of both the surface topography and other quantities (e.g. local dielectric constant).

However, among the different imaging techniques, AFM offers the most versatile platform by combining high resolution and compatibility with different types of samples regardless of other physical attributes. AFM has circumvented resolution limitations introduced by diffraction phenomena, associated with optical tools, or by finite electron escape depth, associated with SEM imaging. In addition, it can image in Air, vacuum, or liquid and generally requires no sample preparation. Moreover, AFM images consist of three dimensional topographic maps of the surface and are, for this reason, ideal for cross sectional metrology applications. These reasons have made the AFM a widely used instrument in many disciplines.

However, despite the AFM's versatility and high resolution, its images are commonly distorted by convolution effects, which become more prominent when the sample surface contains high aspect ratio features. In addition, data artifacts can result from poor dynamic response of the instrument. These two factors will be addressed next in more details.

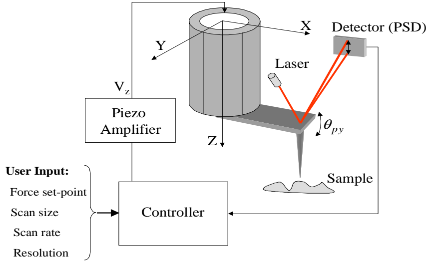

Fig. 1. Schematic diagram of AFM main components.

III. NANO-SCALE IMAGING WITH AFM: TECHNICAL CHALLENGES

An AFM, Fig. 1, consists of a cantilever-mounted probe, a sensor measuring the deflection of the cantilever, and a scanner providing three dimensional relative motion between the probe and a sample. In contact-mode, the probe is brought into contact with the sample, at a user-specified contact force or cantilever deflection. The scanner is then moved in a raster fashion. During scanning, changes in the sample topography change the cantilever deflection. A controller is used to maintain the deflection constant by moving the scanner up and down. The sample image is composed of the correcting voltage sent to the scanner.

A. Image Artifacts Due to AFM Dynamics

Among the factors limiting AFM performance and repeatability are undesirable dynamics of the instrument. This can be attributed partly to user choice of scan parameters (scan speed, force set-point, etc.), and feedback parameters. Usually, AFM users start with some default values of the parameters. In a trial and error manner, parameters are adjusted until a reasonable image is collected. It is therefore of great practical value to be able to select key scan parameters in a systematic and automated fashion. This can improve repeatability, accuracy, and consistency. In addition, it aids in fully automating AFM technology for applications such as quality control in semiconductor industry.

Atomic force microscopes may generate erroneous data. To demonstrate this, a commercial AFM was used to scan a set of Silicon calibration steps. The AFM was run under a proportional-plus integral (PI), control. Scan results demonstrate the high sensitivity of collected images to scan and controller parameters (K_p and K_i). Comparing Fig. 2 (a) (72 $\mu m/s, K_p = K_i = 2$) to Fig. 2 (b) (96 $\mu m/s, K_p = K_i = 20$), some of the effects of scanning speed and controller gains on the image can be seen. Higher gains result in oscillations as the cantilever falls along the right edge of the step, with peaks indicating momentary loss of contact between the probe and the sample. The higher gains improve tracking, as the sharp left edge of the step is resolved more accurately. Fig.'s 3 (a) and (b) were generated with a scan speed of 180 $\mu m/s$ using the same controller gains. The contact force set-point for Fig. 3 (a) is set

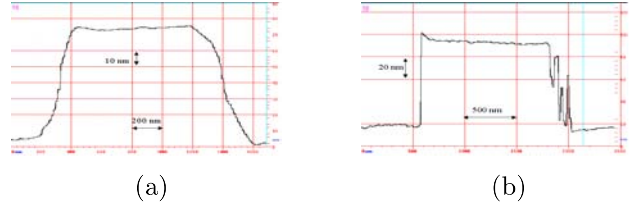

(a) (b)

Fig. 2. AFM images: (a) 72 $\mu m/s$, $K_p = K_i = 2$, (b) 96 $\mu m/s$, $K_p = K_i = 20$.

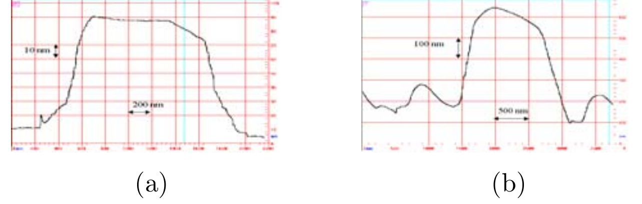

(a) (b)

Fig. 3. AFM images: 180 $\mu m/s$, (a) nominal contact force, (b) smaller contact force.

to the manufacturer's recommended value, while Fig. 3 (b) a smaller force was used. Choosing a small contact force set-point reduces contact deformation and friction, however, it reduces stability of the contact. As seen from Fig. 3 (b), the image generated with a small contact force has erroneous height information, due to loss of contact between the probe and the sample.

Furthermore, there are several factors that limit the AFM performance. The inherent piezoelectric scanner nonlinear sensitivity, hysteresis, creep, and cross-coupling between motion in different axes greatly affect imaging and positioning performance. Presence of creep can introduce artificial shadows and ridges in the image near steep slopes. Moreover, scanner hysteresis can be as much as 25%, and could cause shifts in the image both vertically and laterally. Further, the feedback system can impose additional performance limitations.

One possible approach for improving fidelity and repeatability of AFM images may be through improving its dynamic response by integrating and automating scan parameter selection and control to guarantee consistent performance. Therefore, factors affecting image formation and their impact on performance of the AFM need to be identified and understood. This may be achieved through modeling of the main components of the AFM and the dynamic interactions between them.

B. Image Convolution

Image convolution expresses itself in the form of loss of surface detail and dulling of high aspect ratio features. This type of distortion occurs during the scanning process when the contact point between the probe and the sample is not the apex of the probe but its side instead, as shown in Fig. 4. In other words, during the imaging process, the probe is always externally tangent to the surface,

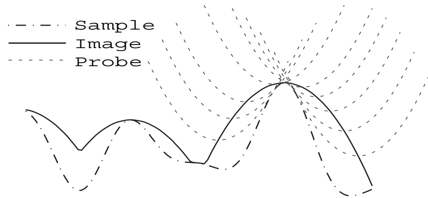

Fig. 4. The probe apex is not necessarily the sole point of contact for high aspect ratio samples. Various positions of the probe along the scan are portrayed.

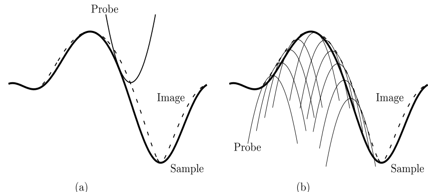

Fig. 5. Mechanism of image formation based on the dilation model. (a) The probe is externally tangent to the sample during the scanning, generating the image. (b) A dual and equivalent interpretation is that the image is the combined volume of the translates of the (reflected) probe.

and as a result, the image is a dilated version of the underlying sample. Dilation distortions introduce errors in the metrology data obtained from the surface [4]. As a result, critical dimensions such as linewidth of steps or radius of curvature of high aspect ratio structures (such as field emission probes and high precision cutting edges) become inaccurate [5].

One mechanism of image formation for AFM is based on the concept of morphological dilation [4], [6], [7]. The image of a sample is a dilated version of the sample and the structuring element is considered to be the reflected probe shape. That is:

$$I = S \oplus \check{P} \tag{1}$$

where $\check{P}$ is the reflected version of the probe shape P, and S is the sample shape and I, the resulting image.

In other words, if one places a copy of the reflected probe on every single point of the sample surface, with the reflected probe apex coinciding with that surface point, then the surface of the resulting combined volume of all translates of these reflected probes will constitute the image of the sample taken with that specific probe (Fig. 5).

A quick analysis of Equation (1) reveals some straightforward conclusions that can be summarized in the following cases:

- Case 1: If the shape of the probe is exactly known and the image is also known, then by applying a reverse mechanism of image formation, the sample shape could be computed, and convolution distortions, eliminated. However, probe estimation is usually inaccurate and ambiguous, especially because probes are prone to wear and dimensional variation due to usage.
- Case 2: Conversely, if the sample shape is exactly known and the image is also known, then by applying a reverse mechanism of image formation, the probe shape could be computed. Likewise, samples whose shape are exactly known in the sub-micron scale are difficult to obtain, characterize and maintain.
- Case 3: If the probe is very sharp compared to the sample dimensions, then the image shape will be very similar to the sample shape, the probe contribution being negligible to image formation. Slender probes, however, are prone to wear and failure and are extremely expensive and difficult to handle. Therefore, their applicability to high volume robust inspection is limited.
- Case 4: Conversely, if the sample is very sharp compared to the probe dimensions, then the image shape will be very similar to the reflected probe shape, the sample contribution being negligible to image formation. The same conclusion stated in Case 3: holds here.

These cases are the basis for existing image deconvolution methods. They all rely on some type of a priori probe information that has to be obtained before the imaging experiment. The probes must be either very sharp or characterized. Characterization standards, however, are difficult to obtain and maintain because typically they must present features much smaller than the employed probes. It would be desirable, then, to develop a methodology that does not require special characterization standards, that can deliver high quality probe estimates for image deconvolution, and that does not reduce throughput or increase complexity significantly.

IV. MODELING AND CONTROL OF AFM DYNAMICS

A. In-contact Dynamics of Atomic Force Microscopes

Previously, we have developed models describing the dynamics of AFM [8], [9], [10]. The main dynamics of interest are those describing the vertical motion, i.e. from the scanner input voltage V_z to the output of the PSD y_{PSD}. A new model for tube scanners used in SPM, and particularly in AFM was developed [9]. The model captures the coupling between motion in different axes as well as a bending motion due to a supposedly pure extension of the tube. It was shown that due to coupling, the bending mode becomes observable from the AFM cantilever deflection sensor output y_{PSD}. This is contrary to the ideal uncoupled case. As a result, the scanner bending mode becomes the primary system resonance instead of the higher-frequency extension mode for the ideal uncoupled case.

Results presented in [10] have shown that changes in contact force set-point or amplitude of disturbance causes changes in DC gain of the frequency response, changes in the frequency of the system zeros, and changes in the resonance peak of system modes. However, the frequency of the bending mode would not be affected as seen in Fig. 6 (a). Physically, this is true since the probe sample forces are orders of magnitude smaller than the force the scanner can provide, ($\sim 10's\, nN$ vs. $\sim 1N$).

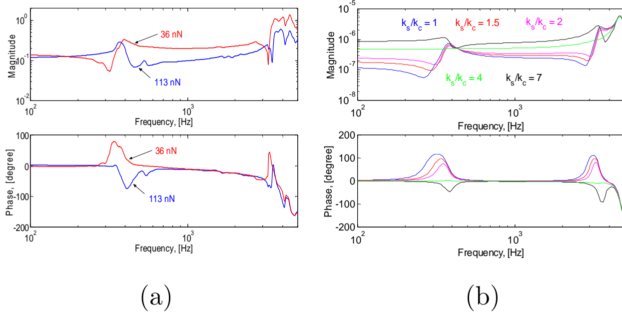

(a) (b)

Fig. 6. (a) Experimental in-contact frequency response with a PDMS sample: $17\,nm$ amplitude for different set-points, (b) Simulated in-contact frequency response for different ratios of sample to cantilever stiffness $\frac{k_s}{k_c}$.

A simulation study was performed to compare the model to experimental data. The model used in this study included four bending modes and two extension modes for the scanner, and one bending mode for the cantilever. The parameter values used are given in [11]. The ratio of sample to cantilever stiffness $\frac{k_s}{k_c}$, proved to be an important parameter. Changes in this ratio have two main effects on the model, namely, change in the transfer function DC gain and changes in the frequency of the zeros associated with the scanner bending modes, $380\,Hz$ and $3.4\,kHz$. Figure 6 (b), shows the simulated frequency response of the model for different ratios of stiffnesses. For large ratios (e.g. $\frac{k_s}{k_c} = 7$), the zeros have a higher frequency than the mode. For smaller ratios (e.g. $1 \leq \frac{k_s}{k_c} \leq 2$), the frequency decreases to be below that of the mode. This change in pole-zero pattern is referred to as pole-zero flipping. Moreover, for some value ($\frac{k_s}{k_c} \approx 4$), there is pole-zero cancelation and the bending modes are unobservable. As a result, as the zeros move away from the mode, the resonance peak appears more prominent in the response. Further, when $\frac{k_s}{k_c}$ is either too large or too small, the DC gain reaches a limit controlled by k_c and k_s, respectively. For intermediate values, the DC gain will depend on both stiffnesses and changes in k_s due to different set-pints or input amplitudes will change the DC gain, and zeros location.

B. Trade-offs and Performance Limitations in AFM Feedback System

When the probe is brought into contact with the sample, the controller should achieve closed loop stability at the desired contact force set-point for the given cantilever and sample. Moreover, the controller should maintain the set-point error within a prescribed tolerance for all times (i.e. transient and steady state), such that probe-sample contact is not lost nor excessive force is applied to the sample. In addition, good dynamic response should be achieved in despite of uncertainties.

It is essential first to identify expected performance trade-offs and limitations. Consider a linear time-invariant (LTI) feedback system of Fig. 7, where d_o is output

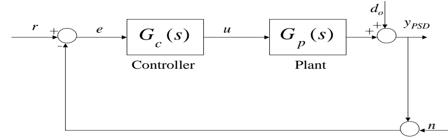

Fig. 7. Block diagram of the AFM feedback system.

disturbance, n is sensor noise, $G_c(s)$ is the controller transfer function, and $G_p(s)$ is the plant transfer function including driving amplifier, scanner, and sensor filter dynamics. The dynamics of typical cantilevers are much faster than scanner lateral dynamics and therefore are neglected. Accordingly, sample topography maybe be modeled as an output disturbance d_o. The image is typically created from the input voltages (u_x, u_y, u_z). Therefore, the transfer functions between d_o and e (sensitivity function $S(s) = \frac{e}{d_o} = \frac{-1}{1+L(s)}$), and between d_o and u (control sensitivity function $S_u(s) = \frac{u}{d_o} = \frac{-G_c}{1+L(s)}$), are the main interest where $L(s) = G_p(s)G_c(s)$. Nominal feedback performance may therefore be specified in terms of $S(s)$ and $S_u(s)$.

The results in [9] have revealed the coupling between the longitudinal and bending dynamics. In addition, the bending modes were found to be observable from the output signal. The frequency of the first bending mode is usually significantly lower than the first longitudinal mode; $380\,Hz$ and $4.6\,KHz$ for the AFM in use. As a result, a substantial reduction in feedback bandwidth is expected as a result of this coupling. Moreover, the poles and zeros of the bending modes will impose additional performance limitations, as will be discussed shortly.

In [10], experiments and simulations have revealed several sources of uncertainties. These changes were found to be a strong function of force set-point and disturbance amplitude. In addition, they may depend nonlinearly on probe-sample contact properties. These large variations and uncertainties would generally result in trading-off bandwidth (performance) to guarantee robust stability or performance. This point will be demonstrated using two experimental frequency responses. The two responses were obtained for the same disturbance input amplitude but for two different force set-points, namely, 36 and $113\,nN$. An integral controller $G_c(s) = \frac{k_i}{s}$ is used. The controller gain was chosen to achieve a crossover frequency of $93\,Hz$ and $112\,Hz$ for the $36\,nN$ and $113\,nN$ data, respectively. Figures 8 (a) and (b), show S_u and $S(s)$, respectively, for both force set-points. For the smaller force, pole-zero flipping occurs resulting in a very large peak close to the frequency of the bending mode. As a result, poor robustness properties and performance is expected; despite a relatively low bandwidth compared to the open loop bending resonance at $380\,Hz$. An image taken under these conditions would show oscillation if the probe would be perturbed during scanning. This is demonstrated in Fig. 9, where an experimental AFM image of a $1046\,nm$

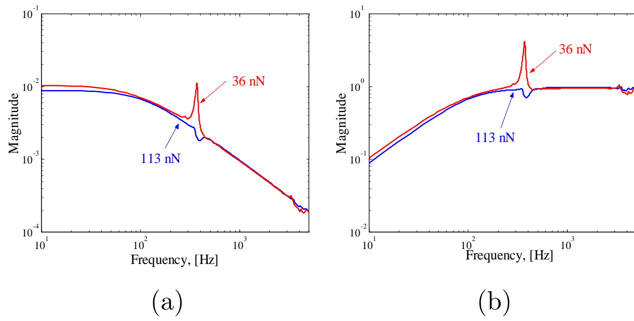

Fig. 8. Experimental frequency response data with integral control, (a) Control sensitivity function, (b) Sensitivity function.

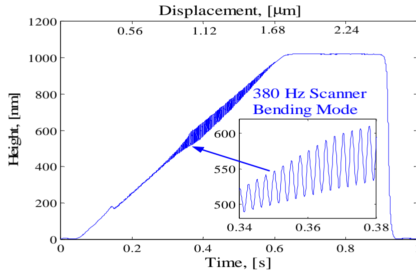

Fig. 9. Oscillations due to scanner bending mode in experimental AFM image of a 1046 nm Silicon step.

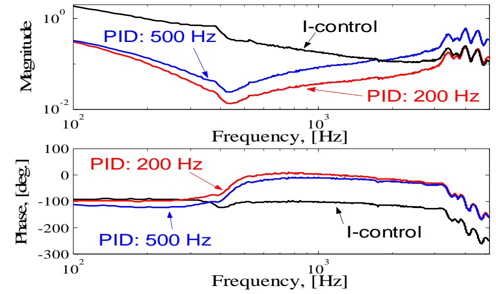

Fig. 10. Loop transfer function frequency response with integral control and proper PID controller.

step is shown. A small force helps reduce probe-sample friction, sample deformation hence, image distortion. However, it may dictate a small bandwidth in order to eliminate oscillations in the image, therefore, trading off bandwidth (performance) for robustness.

It was shown in [12], [11] that the presence of zeros in an LTI system may impose a fundamental trade-off between response time and overshoot. For the AFM feedback system [11] it was shown that extending the bandwidth beyond the first scanner bending mode will result in overshoot in tracking step-like samples in both output and voltage (image signal), responses. It was also shown that this limitation can not be alleviated by the controller canceling the zeros nor by adding a scanner vertical displacement sensor and generating the image from its signal.

C. Performance of PID Controllers

As mentioned previously, substantial increase in the feedback bandwidth beyond the first resonance will result in overshoot and poor time response. In order to reduce the effect of high-frequency modes on feedback stability and performance, the relative degree of the loop transfer function should be made one or higher by the controller. Commercial AFM use a PID controller . Due to the aforementioned high-frequency roll-off constraint, in addition to the performance constraint mentioned above, it was found that a PID controller does not provide any advantage over a simple integral controller. Figure 10, compares the experimental frequency response of the loop transfer function for both integral and a proper PID controller (with one extra pole). The PID controller zeros were set at 400 Hz, only 5% from the actual resonance. Two cases are shown, one with a pole at a lower frequency than the resonance frequency (at 200 Hz), while in the other case the pole frequency is higher (at 500 Hz). It is seen that the crossover frequency for both PID controllers is about 30 Hz, while for integral control it is 200 Hz. Hence, a PID would trade-off bandwidth in order to meet the high-frequency modes constraint. In addition, a standard improper PID controller would achieve an even smaller bandwidth.

D. Automated Selection of Scan Parameters

An algorithm for automatic selection of scan parameters using integral control was developed. The algorithm estimates in real-time several key system parameters and does not rely on nominal or catalog values of any parameter. These estimates are used to provide appropriate values for force set-point, integral gain, and a range of scan speed. The algorithm tries to utilized the smallest contact force set-point as possible and then tries to maximizes the feedback bandwidth. A range of scan speeds is then given. Ambiguity arises in which scan speed to choose. Using a small scan speed would yield better image but would require longer time to complete a scan. On the other hand, using the smaller scan speed may be too conservative. To mitigate this problem, two additional algorithms were developed. One algorithm relies on using a fixed value for scan speed such as the average value, and modifying the control law to improve the image. The second algorithm varies the scan speed based on real-time estimation. With the presence of creep in the piezoelectric scanner images taken at different scan speeds could result in changing the lateral scale of the image. However, a method for creep compensation both in lateral and height was also developed [11]. Hence, improving the robustness of the variable scan speed algorithm. Among both algorithms, it was found that the latter is more general and robust.

The proposed procedure for automatic scan parameter selection was tested experimentally. The performance of the I-controller with the proposed tuning procedure was compared with the PID controller used with commercial

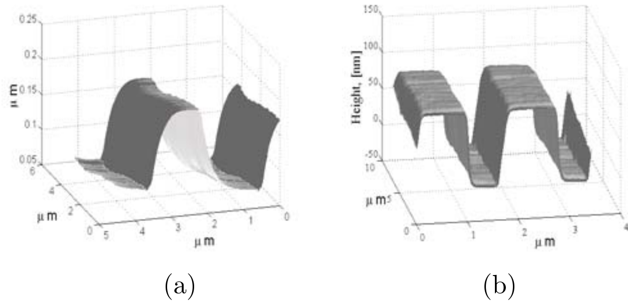

Fig. 11. AFM images of Silicon steps: (a) PID controller with default parameter values, (b) I-controller using proposed tuning method.

AFMs. A set of Silicon steps were imaged. More details are available in [11]. The resulting images are shown in Fig. 11 (a) and (b) for the PID and I controller, respectively. As clearly seen from the figures, the I-controller provides a more accurate image of the steps while using a substantially smaller contact force and hence reducing the probe-sample friction force. As a result, more details on the sample surface quality can be observed while reducing the possibility of sample and probe damage and wear. Moreover, as discussed in Section IV-C the I-controller can achieve a higher feedback bandwidth than the PID controller, therefore, a much smaller scan rate compared to that used with the I-controller would be required with the PID controller to resolve the sample shape accurately.

E. New Method for Scanner Calibration

The accuracy of AFM data ultimately depends on the calibration of the scanner. Piezoelectric materials exhibit nonlinear quasistatic voltage to displacement response. Nonlinearity of 20 to 25 % is expected for soft piezoelectric materials generally used in SPM. Calibration of the scanner is usually performed by imaging a standard sample with a known characteristic dimension. The voltage to displacement sensitivity is then computed from the applied voltage and the known dimension(s) of the standard and a linear sensitivity is assumed for vertical calibration. However, utilizing images for calibration could be problematic for vertical calibration. Standards with a small height compared to the scanner range, are commonly used for calibration to reduce the effect of hysteresis. Consequently, calibration would only be accurate for a small fraction of the total scanner range (typically $\sim 3\%$). Imaging samples with features taller than the standard used for calibration will be corrupted with both hysteresis and nonlinearity due to the scanner's displacement. As a results of our work, a new method for calibrating the scanner's full range vertical displacement has been developed. The method can also be used for identifying scanner hysteresis in the vertical direction. Once identified, hysteresis can be compensated for.

V. IMAGE DECONVOLUTION: STEREO IMAGING

We propose a new approach to image deconvolution called Stereo Imaging. In this approach, two images of the same sample are obtained at different vantage points. That is, the sample is mechanically rotated relatively to the probe prior to the second scan. Since the rotation angle can be specified, one obtains the following system of equations:

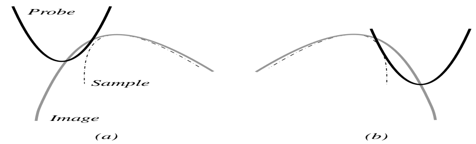

Fig. 12. Two images from different vantage points. (a) Sample tilted by $-\pi/10$ radians and resulting image obtained with the portrayed probe. (b) Second image obtained by rotating the sample by $\pi/10$ radians from the vertical direction. Both images are blunt and distorted versions of the high aspect ratio sample due to convolution.

$$\begin{aligned} I_1 &= S \oplus \check{P} \\ I_2 &= S^* \oplus \check{P} \\ S^* &= Rot(S, \theta) \end{aligned} \tag{2}$$

If S is the set of all points $\{x, y\}$ pertaining to the surface of the sample, then S^* will be composed of points $\{x_r, y_r\}$ as determined by the rotation operator shown in Equation (3).

$$\left\{ \begin{array}{c} x_r \\ y_r \end{array} \right\} = \left[\begin{array}{cc} \cos(\theta) & -\sin(\theta) \\ \sin(\theta) & \cos(\theta) \end{array} \right] \left\{ \begin{array}{c} x \\ y \end{array} \right\} \tag{3}$$

Equation (2) defines a system with two equations and two unknowns and therefore can be solved for both probe and sample geometry without the need for prior characterization. The rotation of the sample provides an extra constraint for estimation; as a result, estimation ambiguity is greatly reduced.

The steps involved in stereo imaging include: (1) obtaining two images of the sample; (2) roughly estimating the probe shape by blind deconvolution. Complete discussions on rough blind estimation can be found in [7], [13], [14] and [15]; (3) combining probe estimates by overlay; (4) generating sample estimates by Erosion; (5) combining sample estimates by overlay; (6) sharpening the probe estimates. Steps (3) though (6) are repeated until convergence is reached. Further explanations follow.

The first step of the methodology consists of obtaining two images of the same sample at different angles as seen in Fig. 12. The sample rotation is obtained by means of a high precision tilt actuation system. In this example, the sample is chosen to have a high aspect ratio. Notice how the images are blunter and wider versions of the underlying sample due to convolution. Also, in this example, in the first image the sample is tilted by $-\pi/10$ radians and in the second image, the sample is tilted by $\pi/10$ radians. Next, blind deconvolution is used to estimate the probe geometry for each image. The estimates are combined by simply overlaying them. A sharper estimate

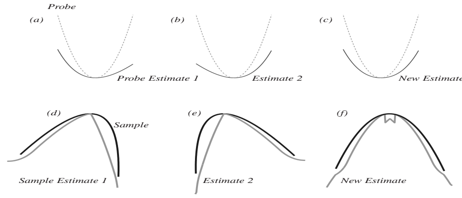

Fig. 13. Probe and sample initial estimation. (a) and (b) portray the results of probe estimation by blind deconvolution for each image. The estimates are significant different than the original probe shape. In (c), estimate combination yields a slightly tighter estimate. (d) and (e) are sample estimations for each vantage point obtained by erosion with the new combined probe estimate. (f) shows the new sample estimate by overlay of the previous estimates. This estimate is somehow closer to the real sample shape but far from precise.

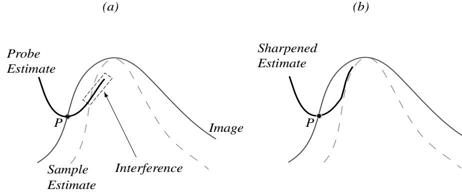

Fig. 14. (a) Probe Estimate must be always externally tangent to sample estimate in order to satisfy Equation (1). Therefore, the interfering region must be trimmed from the probe estimate. As a result, the probe estimate is sharpened as shown in (b).

for the probe is obtained. This probe estimate is used to generate sample estimates based on each image. The process of sample estimation given a probe estimate is called Erosion and corresponds to the inverse mechanism of image formation. Complete discussions on Erosion can be found in [7], [13], [14] and [15]. The sample estimates are combined to generate a new one by simply overlaying them as shown in Fig. 13(f). Now, the new probe estimate must be sharpened in order to satisfy Equation set (2). The process of sharpening the probe estimate includes the following steps: (1) Place probe estimate in a certain point P_1 along the image. (2) Verify if the probe estimate interferes with the sample estimate. (3) Trim or sharpen interfering regions of the probe. (4) Repeat procedure for all points P_i along one image. (5) Repeat procedure for the second image. The sharpening procedure makes sure that each image is a dilation of the estimated sample by a structuring element with the shape of the reflected probe estimate. That is, it forces the estimates to satisfy Equation set (2). The sharpening operation reduces ambiguity around sample and probe estimation. This is so because the space of solutions for probe and sample geometry satisfying one constraint as established in Equation (1) is necessarily larger than the space of solutions that satisfy two constraints, simultaneously, as established in Equation set (2). Consequently, increasing the number of constraints (or images at different angles) will eventually reduce the space to a single solution and zero ambiguity. However, multiple imaging is too time consuming and two images seem enough to accomplish high precision estimates in most cases. The sharpened probe estimates are then combined by overlay again. New

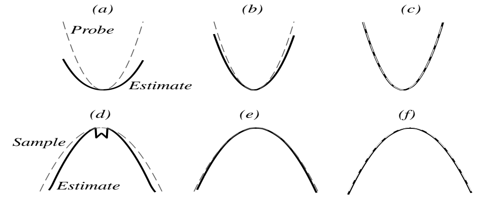

Fig. 15. Evolution of estimates. Sketches (a) and (d) show probe and sample estimates based on a combination of blind estimates. Since the sample is not very sharp, estimates are very inaccurate. Sketches (b) and (e) are the results of the first iteration of the Stereo Imaging procedure. Estimates are greatly enhanced. Sketches (c) and (f) are the results of the second iteration. Estimates and real geometries are identical; convergence is reached and no significant geometrical changes happen in further iterations.

sample estimates are generated by erosion and the whole process is repeated until no noticeable change in the estimates is detectable. That is, until the RMS of the difference between probe estimates from one iteration to another is sufficiently small. The evolution of probe and sample estimates is shown in the Fig. 15.

As a conclusion, by obtaining two or more images of the sample at different vantage points, stereo imaging can be used to generate high precision estimates of both probe and sample simultaneously. Therefore, metrology accuracy is ensured, regardless of probe shape or size. Since the probe geometry is estimated at every imaging event, an effective probe monitoring scheme can be implemented. Since all steps involved in the Stereo Imaging approach are carried out by set or morphological operations, its generalization to 3-D and volume analysis (instead of the cross-sectional analysis discussed in this paper) is simple. This methodology has been applied to image deconvolution of high aspect ratio features such as silicon gratings and industrial blades with success. Validation included direct comparisons to white light interferometry and SEM imaging data. The experimental tests and results are available elsewhere [3].

One of the proof of concept studies included the imaging of high aspect ratio high precision standards. The stereo imaging algorithm was used to reconstruct the probe geometry as well. The reconstruction results were compared to both SEM and high precision grating images and showed great similarity. From the probe estimation experiments, the following conclusions can be drawn.

- The included angles of the probe reconstructions were very close to the theoretical angle of 70° demonstrating the accuracy of the methodology (Fig. 16).
- The reconstruction profiles for all 4 samples are very similar, demonstrating the repeatability of the technique and its invariance to different sample shapes (Fig. 16).
- The radius of curvature of the probe reconstructions are very similar, demonstrating the repeatability of the stereo technique. The radius was calculated by

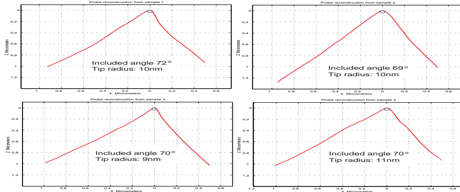

Fig. 16. Probe estimates corresponding to the four different samples.

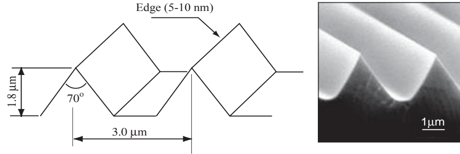

Fig. 17. Silicon grating and dimensions. From NT-MDT.

fitting a circle to the image apex, a procedure that may introduce small numerical discrepancies.

An indirect verification of the probe reconstruction quality was carried out using high precision standard gratings. The gratings are similar to the one shown in Fig. 17. They are produced by preferential etching of silicon and have an included angle of 70°. In addition to that, the manufacturer's data indicates that the radius of curvature of the grating should be around or smaller than 5nm. Therefore, the AFM image of a grating should have an average convolved radius of curvature R_i equal to the sum of the radius of curvature of the grating R_g and the radius of curvature of the probe R_p. In fact, after imaging the grating, Fig. 18, the image was found to have $R_i = 14.3nm$ which is approximately $R_g + R_p \approx 5nm + 10nm$. Finally, a direct verification was done by comparing the probe reconstructions with an SEM image of the probe. However, the probe had to be coated with an approximately 10nm thick gold film for contrast enhancement. Therefore, this comparison is simply qualitative. The overlay of probe estimate and SEM image showed striking similarity, a further evidence of the accuracy of the stereo estimation

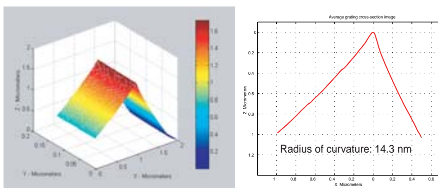

Fig. 18. High precision standard grating image and averaged cross-section.

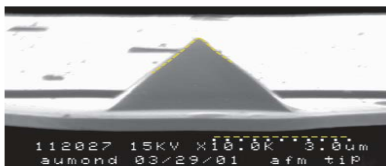

Fig. 19. Overlay of probe reconstruction corresponding to sample 3 and SEM view of the same probe.

method. One such overlay is shown in Fig. 19.

VI. CONCLUSION

A review of different technologies used for obtaining high precision 3-D images of surfaces were presented. Among different imaging techniques AFM offers the most versatile platform by combining high resolution and compatibility with different types of samples and operating media. However, AFM images are commonly distorted by convolution effects, which become more prominent when the sample surface contains high aspect ratio features. In addition, data artifacts can result from poor dynamic response of the instrument. In order to achieve reliable data at high throughput, dynamic interactions between the instrument's components need to be well understood and controlled, and novel image deconvolution schemes need to be developed. A summary of our work at mitigating these distortions was presented.

The authors greatly appreciate the support of the Singapore-MIT Alliance program.

References

[1] S. I. Association, International Technology Roadmap for Semiconductors: 2000 update. Austin, TX: International SEMATECH, 2000.

[2] D. G. Chettwynd and S. T. Smith, "High precision surface profilometry: From stylus to stm," From Instrumentation to Nanotechnology.

[3] B. Aumond, High Precision Stereo Profilometry. Mechanical Engineering PhD. Thesis, MIT, Cambridge, Massachusetts, June 2001.

[4] G. Pingali and R. Jain, "Restoration of scanning probe microscope images," Proc. IEEE Workshop on Applications of Computer Vision, pp. 282–289, 1992.

[5] B. Aumond and K. Youcef-Toumi, "High precision stereo profilometry based on atomic force microscopy technology," Proceedings of the Mechatronics 2000 Conference, Atlanta, Georgia, September, 2000.

[6] J. Villarubia, "Reconstruction of stm and afm images distorted by finite-size tips," Surface Science, vol. 321, pp. 287–300, 1994.

[7] Y. Yeo, "Image processing for precision atomic force microscopy," Mechanical Engineering M.S. Thesis, MIT. Cambridge, Massachusetts, June 2000.

[8] O. M. E. Rifai and K. Youcef-Toumi, "Dynamics of contact-mode atomic force microscopes," American Control Conference, Chicago, Illinois, USA, June 28-30, pp. 2118–2122, 2000.

[9] ——, "Coupling in piezoelectric tube scanners used in scanning probe microscopes," American Control Conference, Arlington, Virginia, USA, June 25-27, pp. 3251 –3255, 2001.

[10] ——, "Dynamics of atomic force microscopes: Experiments and simulations," IEEE Conference on Control Applications, Scotland, Setember 18-20, pp. 1126–1131, 2002.

[11] O. M. E. Rifai, Modeling and Control of Undesirable Dynamics of Atomic Force Microscopes. Mechanical Engineering PhD. Thesis, MIT, Cambridge, Massachussets, February 2002.

[12] G. Goodwin, A. Woodyatt, R. Middleton, and J. Shim, "Fundamental limitations due to $j\omega$-axis zeros in siso systems," Automatica,, vol. 35, pp. 857–863, 1999.

[13] J. S. Villarubia, "Scanned probe microscope tip characterization without calibrated tip characterizers," J. Vac. Sci. Technol. B, vol. 14 (2), pp. 1518–1521, 1996.

[14] P. M. Williams, K. M. Shakesheff, M. C. Davies, D. E. Jackson, C. J. Roberts, and S. J. B. Tendler, "Blind reconstruction of scanning probe image data," J. Vac. Sci. Technol. B, vol. 14 (2), pp. 1557–1562, 1996.

[15] S. Dongmo, M. Troyon, P. Vautrot, E. Delain, and N. Bonnet, "Blind restoration method of scanning tunneling and atomic force microscopy images," J. Vac. Sci. Technol. B, vol. 14 (2), pp. 1552–1556, 1996.